LCLS-II Technical Note

LCLS-II Gun-2 RF Design Analysis

LCLS-II TN-22-02

10/21/22

Liling Xiao, Chris Adolphsen, Erik Jongeward, Xianghong Liu and Feng Zhou

LCLS-II Gun-2 RF Design Analysis

Liling Xiao, Chris Adolphsen, Erik Jongewaard, Xianghong Liu and Feng Zhou

Contents

Definitions

Parameters	**Definitions**
σ (S/m)	Electrical conductivity
ε_r	Relative permittivity
κ *(W/m K)*	Thermal conductivity
α (1/K)	Thermal expansion
h (W/m^2 K)	Convective heat transfer coefficient
λ (N/m^2)	The first Lamé parameter
μ (N/m^2)	The second Lamé parameter
Cu	Copper
SS	Stainless steel
Al	Aluminum
Mo	Molybdenum
Ec	Electric field at the cathode center
LCW	Low conductivity water

1. RF Parameters

The LCLS-II AIP spare gun (Gun-2) design is largely based on the existing LCLS-II gun (Gun-1), which was designed and built at LBNL. To help suppress dark current, the Gun-2 cathode and anode nose and the cathode plug opening are elliptically shaped to minimize the peak surface field for a given cathode gradient [1][2]. The Gun-1 and Gun-2 2D shapes are shown in Figure 1.

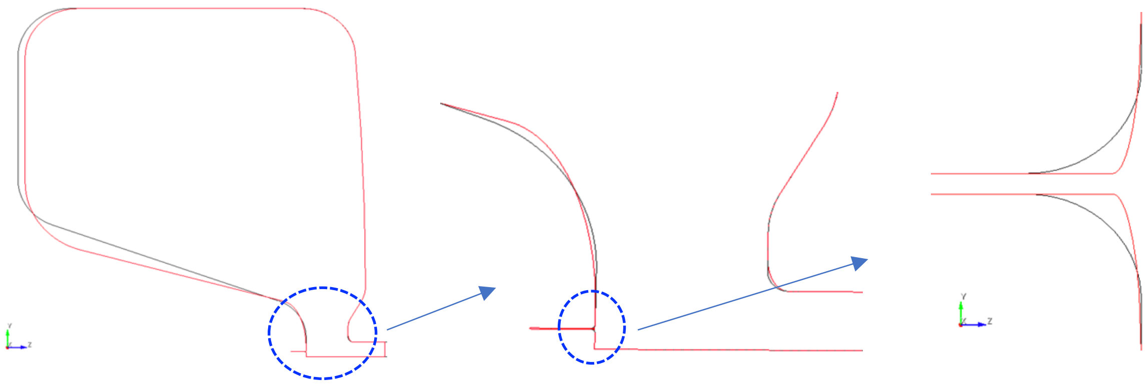

Figure 1: Gun-1 (black) and Gun-2 (red) 2D geometries (left) and the zoomed-in cavity gap (middle) and the cathode plug opening (right).

The SLAC parallel finite-element electromagnetics code suite ACE3P was used to model the RF, thermal and structural properties of the guns [3]. Figure 2 shows the resonant mode electric and magnetic fields obtained from the ACE3P eigen-solver program Omega3P in a one-sixteenth azimuthal slice of the Gun-2 geometry with a shorted, 15-mm long cylindrical gap between the cathode plug and nose.

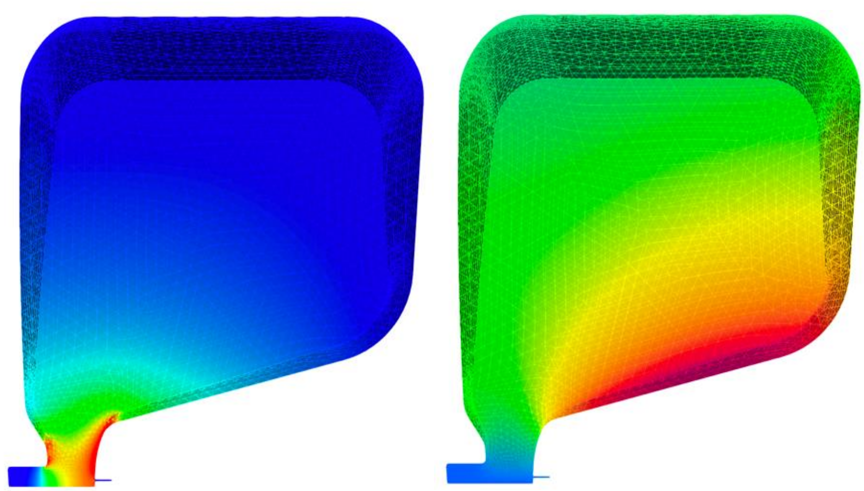

Figure 2: Electric (left) and magnetic (right) fields in a one-sixteenth azimuthal slice of Gun-2.

The Gun-1 and Gun-2 RF parameters are listed in Table 1. The peak electric field in the Gun-2 is lower by 10%.

Table 1: Gun-1 and Gun-2 RF Parameters for a 750 keV Energy Gain

Cavity parameter	**Gun-1**	**Gun-2**
Frequency (MHz) in 2D gun model	186.850	186.018
Nominal cathode-to-anode gap (mm)	40	40
Quality factor Q_0	~$3.12\text{x}10^4$	~$3.12\text{x}10^4$
Shunt impedance R/Q (Ω)	202	208
Electric field (MV/m) at cathode center Ec	19.5	19.8
Peak electric field (MV/m) on cavity nose	24.2	21.8
Peak electric field (MV/m) near cathode plug gap opening on cathode nose	23.2	21.0
Peak electric field (MV/m) near cathode plug gap opening on cathode plug	23.8	21.0
Peak electric field (MV/m) on anode nose	24.4	21.6
Total RF power loss (kW)	87	85

The Gun-1 2D model frequency is about 910 kHz higher than optimal based on our analysis. As a consequence, during the gun fabrication, which involved adjusting the cathode-to-anode gap to achieve a target frequency, the gap that resulted was likely 38.3 mm (i.e., not the 40 mm design value). The shorter gap increased the peak surface electric field by 5% compared to that in the Gun-1 2D model.

2. Stainless Steel (SS) Inserts

In Gun-1, there is significant captured dark current that originates on the high field copper (Cu) surface near the plug gap opening. Using stainless steel (SS) inserts in this region should reduce such current as SS has a lower potential for field emission (no emission is seen from the Mo plug in Gun-1). For this purpose, Gun-2 will have the SS inserts shown in Figure 3, which are also used in the high field anode nose region.

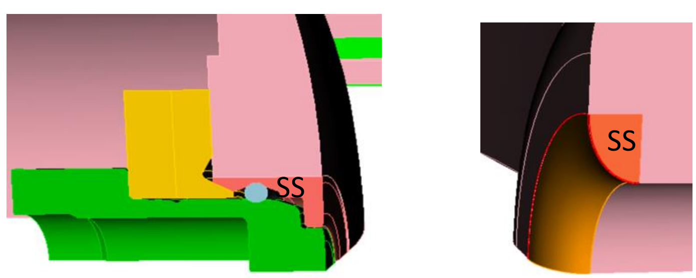

Figure 3: Cathode (left) and anode (right) SS inserts.

The surface electric and magnetic fields around the two SS inserts are plotted in Figure 4. The electric and magnetic fields are normalized to Ec, the electric field at the cathode center. The total RF loss on the SS inserts is about 22 W for a 750 keV energy gain. Increasing the radius of the inserts would rapidly increase the heating as the magnetic field increases with radius.

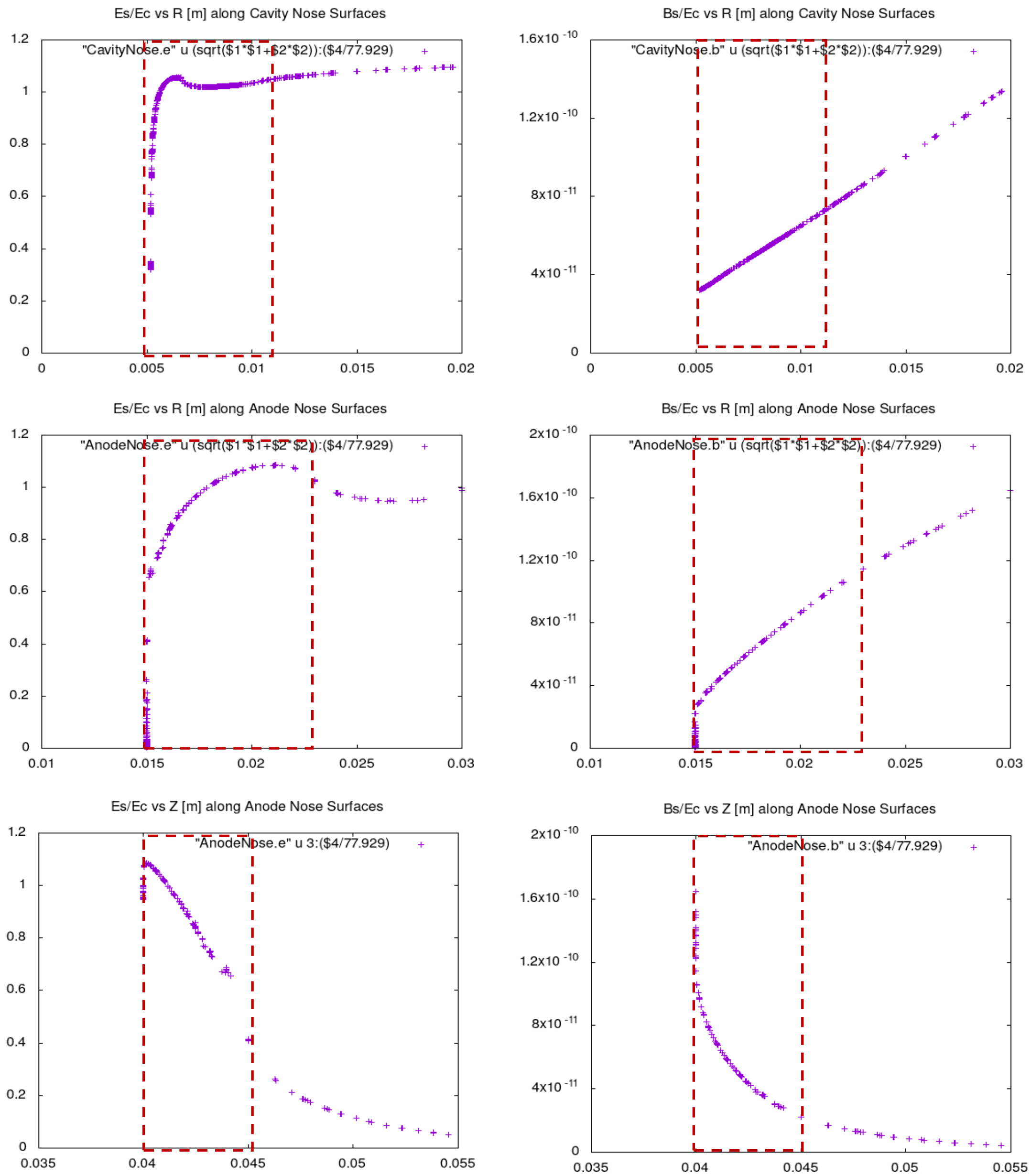

Figure 4: The electric and magnetic fields on the cavity surfaces around the two SS inserts, which span the distance between the red vertical dashed lines.

3. Frequency Sensitivities to Cavity Dimensions

Changing the depth of cathode back plane changes the cavity frequency without impacting the field in the gap region. Varying this depth was used to tune the cavity frequency during the design phase. Moving the anode plate relative to the cathode section changes both the cavity frequency and field in the gap region, and provisions will be made to allow small (~ 1 mm) gap changes during fabrication to fine tune the gun frequency before the anode plate is clamped to the cathode section. The cavity frequency sensitivities to the cavity dimensions are listed in Table 2.

Table 2: Frequency Sensitivities to Cavity Dimensions

Dimension change	**Frequency sensitivity**
Move cathode back plane away from cathode nose	-339 kHz/mm
Move anode plate away from cathode section	541 kHz/mm
Increase cavity outer radius	-64 kHz/mm

4. Frequency Corrections

4.1 Air Relative Permittivity

When the cavity is filled with air, the relative permittivity of the interior is 1.0006. The simulated cavity frequency is 56 kHz lower in air than under vacuum.

4.2 Cathode Plug

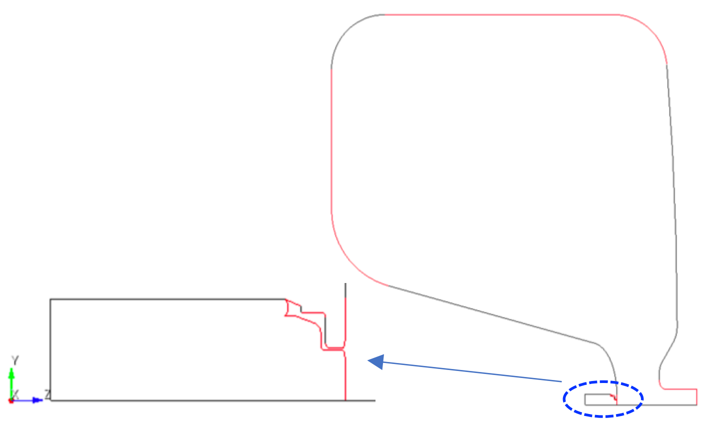

Figure 5: The 2D shapes with (red) and without (black) the cathode plug inserted.

The Gun-2 2D shapes with and without the cathode plug are shown in Figure 5. Without the plug, cavity frequency increases by 6 kHz. The cavity frequency sensitivity to the cathode plug longitudinal position relative to nominal is 5.6 kHz/mm within 0.1 mm range as listed in Table 3. The field enhancements due to plug misalignments in the longitudinal and transverse directions are listed in Tables 4 and 5, respectively.

Table 3: Cathode Plug Related Frequency Sensitivity

Plug location	**Frequency change**
Without cathode plug	6 kHz
With cathode plug retracted	5.6 kHz/mm

Table 4: Field Enhancement due to Cathode Plug Longitudinal Misalignments

Peak E/Ec location	**Nominal z = 0**	**Insert plug z = +0.1 mm**	**Retract plug z = -0.1 mm**
Cavity nose near the plug opening	1.06	1.04	1.07
Cathode near the plug opening	1.06	1.10	1.02

Table 5: Field Enhancement due to Cathode Plug Transverse Misalignments

Peak E/Ec location	**Plug centered radially**	**Plug radial offset by +0.05 mm**
Cavity nose near the plug opening	1.06	1.06
Cathode near plug opening	1.06	1.06

4.3 3D Features

4.3.1 Vacuum Slots

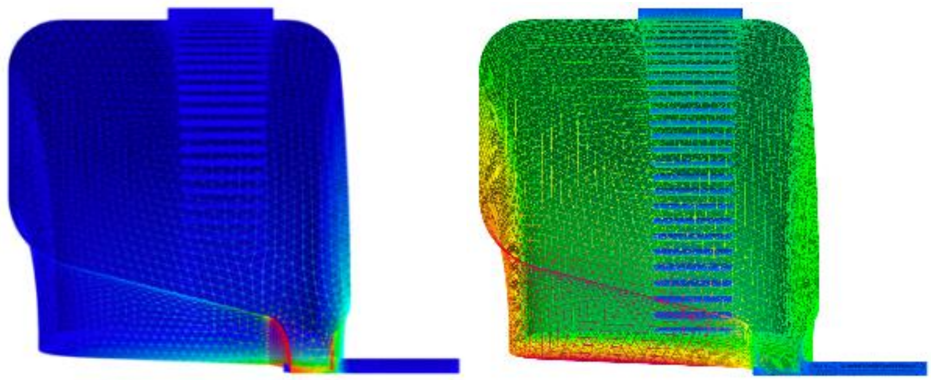

Figure 6: The electric (left) and magnetic (right) fields in a quarter of the Gun-2 cavity without the input couplers, probe ports and viewports.

There are 104 vacuum pump slots on the Gun-2 cavity wall (same as for Gun-1). Figure 6 shows the fundamental mode electric and magnetic fields in a quarter of the gun geometry with the slots and the cathode plug. The presence of the slots reduces the cavity frequency by 64 kHz.

4.3.2 Input Couplers and Small Ports

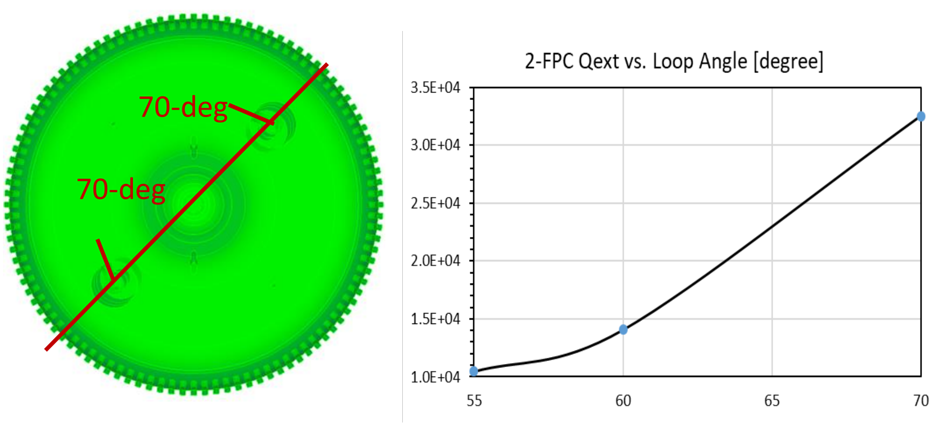

Figure 7: The Gun-2 3D geometry showing the couplers and their loop orientations (left) and Qext versus the loop angle in degrees (right).

The cavity has two identical loop fundamental power couplers (FPCs), which are of the same design as used in Gun-1. As shown in Figure 7, the angles of the FPC loop antennas were adjusted to achieve critical coupling with fixed antenna intrusions of 4.47 mm, that is $Qext = Q_0$, where $Q_0 = \sim 3x10^4$ is cavity quality factor Q_0. The 3D model also included the two probe ports and two view ports.

The resonant mode electric and magnetic fields for critical coupling are shown in Figure 8 for a loop angle of 70°. The frequency is 162 kHz lower due to the couplers and the additional ports. Removing the antennas and blanking off the ports reduces the cavity frequency by 40 kHz. The resonant mode electric and magnetic fields in this case are shown in Figure 9.

The Gun-2 3D half-model geometry without the probe and view ports was simulated using both Omega3P and the ACE3P S-parameter solver S3P. The simulated reflection coefficient from the input coupler is shown in Figure 10. The resonant mode frequencies from these two programs differ by only 3 kHz. The cavity wall is treated as an impedance boundary in S3P, and as a perfect electric boundary in Omega3P. The quality factor was calculated based on the surface magnetic field computed by Omega3P. There is a 6 kHz frequency difference between the half and full models, which is caused by the probe and view ports.

Table 6 and Table 7 summarize the frequency results and changes for the various configurations discussed above.

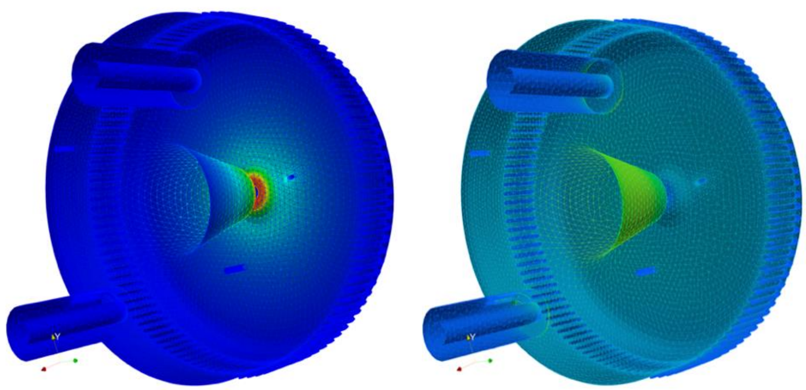

Figure 8: The complex electric (left) and magnetic (right) fields in the Gun-2 full 3D geometry.

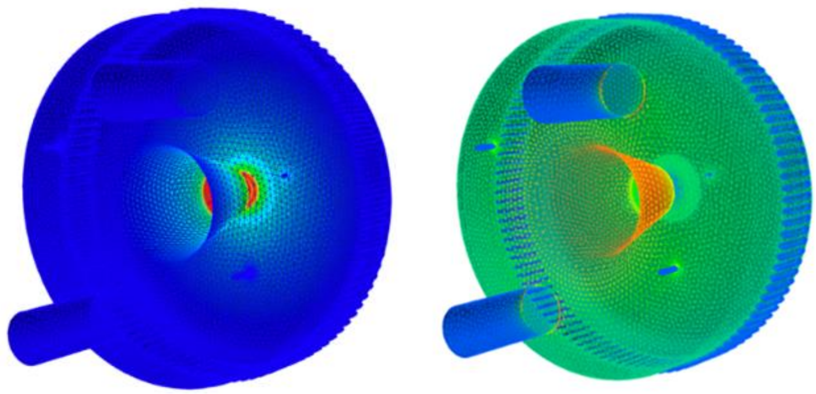

Figure 9: Gun-2 resonant mode electric (left) and magnetic (right) fields sans couplers with the coupler ports blanked off.

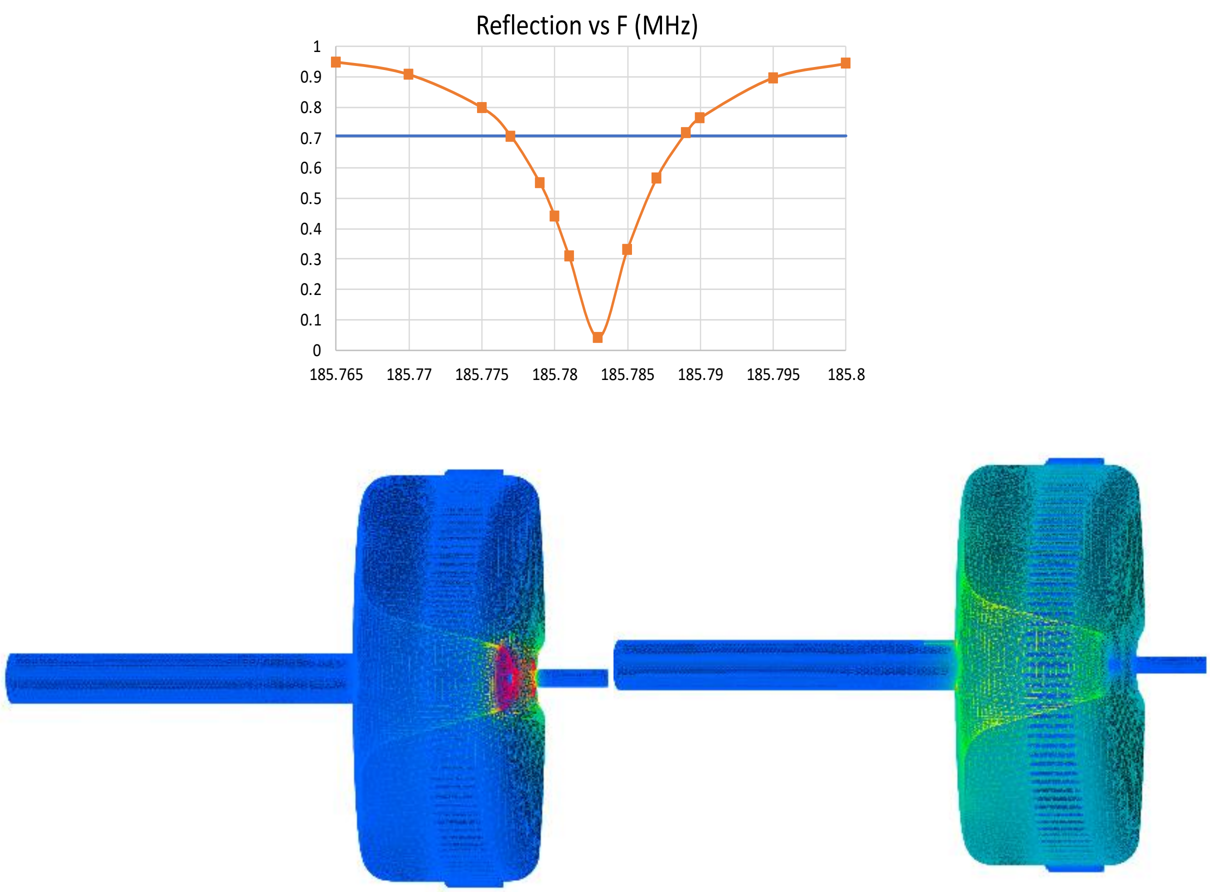

Figure 10: The reflection coefficient from the input coupler in the half model without the probe and view ports (top), and the resonant mode electric (lower left) and magnetic (lower right) fields.

Table 6: Frequencies for Different Configurations

Configuration change	F (MHz)	Q_0	Qext	Frequency change
3D quarter model with vacuum slots and realistic cathode plug	185.954	31659	N/A	-64 kHz due to vacuum slots
Full 3D model including all 3D features, matched FPC ports	185.792	31196	32504	-162 kHz due to FPCs, probe and view ports
Full 3D model w/o antennas, shorted FPC ports	185.752	31598	N/A	-40 kHz due to coupler antenna removal
2D model with a 15-mm long cylindrical plug gap	185.018	31258	N/A	0

Table 7: Frequency Changes

Change from the base 2D model	Frequency change
3D features including vacuum slots and probe and view ports. No coupler antennas, shorted coupler ports	-266 kHz
Insert coupler antennas with 4.47 mm antenna intrusions and 70^{o} angles, matched FPC ports	+40 kHz
Insert realistic cathode plug	-6 kHz
With vacuum slots	-64 kHz
Change permittivity (ε_r) from 1.0006 (air) to 1.0 (vacuum)	+56 kHz

5. Uniform Temperature Change

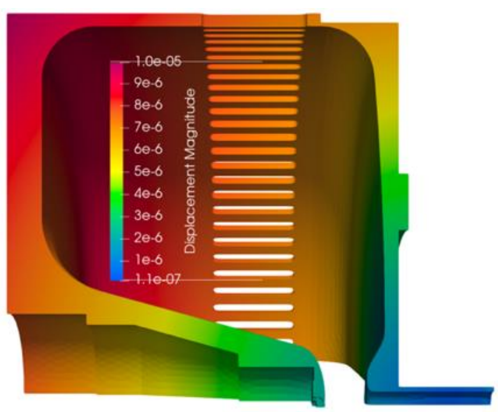

Figure 11: The displacements due to a uniform 1 ^{o}C temperature increase.

The Gun-2 cavity frequency change due to thermal expansion was simulated using the ACE3P multi-physics solver Tem3P with the assumption that the thermal expansion of copper is 1.77e-5/K. The end of beampipe was fixed in the longitudinal (z) direction and thus serves as the reference point. The outer 'jacket' of the cavity that is used for vacuum pumping, clamping and stiffening was not included.

The displacements resulting from a uniform 1 ^{o}C temperature rise are shown in Figure 11. The change in frequency yields a temperature sensitivity of -3.3 kHz/^{o}C. Since the gun model in this case is basically just the copper part, the sensitivity equals the copper thermal expansion coefficient times the gun frequency – including the SS vacuum pumping jacket in the model does not change the results significantly.

6. Atmospheric Pressure

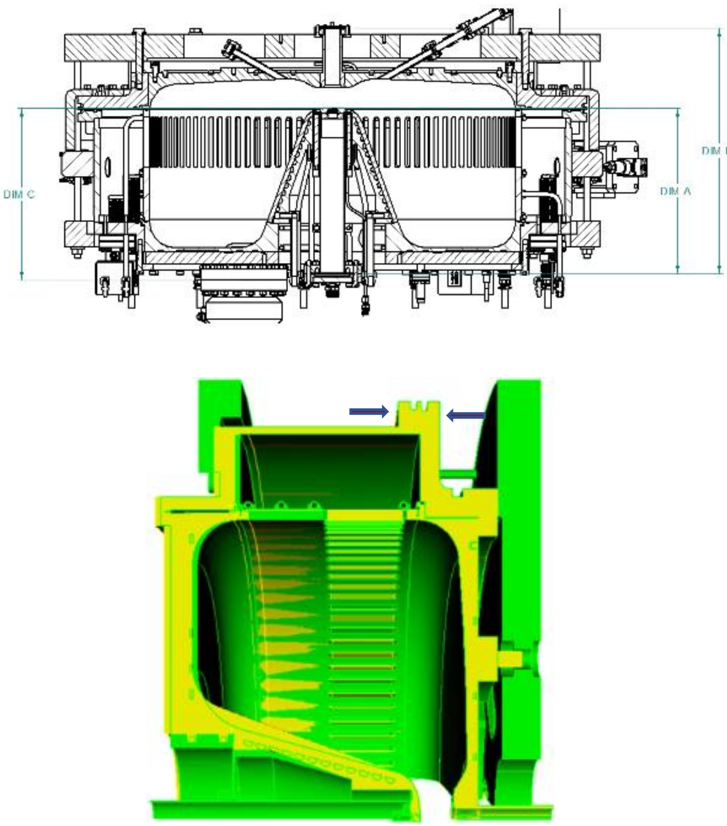

Figure 12: Gun-1 cross section (up) and an overlay of the Gun-1 (yellow) and Gun-2 (green) solid models (down) not including the clamps at the weld joint where the arrows point to.

The Gun-2 engineering design tries to maintain the overall dimensions of Gun-1 so it will be plug compatible with Gun-1. In particular, the dimensions DIM-A, DIM-B and DIM-C shown for Gun-1 in Figure 12 are similar for Gun-2 [4]. However, there are some minor differences due to the improvements that were made, which are illustrated in Figure 12 by the overlay of the two simulation models. The material properties used for the structural analysis are listed in Table 8.

Table 8: Material Properties

Materials	$\boldsymbol{\kappa}$ **(W/m K)**	$\boldsymbol{\mu}$ **(N/m²)**	$\boldsymbol{\lambda}$ **(N/m²)**	$\boldsymbol{\alpha}$ **(1/K)**	$\boldsymbol{\sigma}$ **(S/m)**
Cu	391	4.51×10^{10}	7.16×10^{10}	1.77×10^{-5}	5.8×10^{7}
Al	150	2.78×10^{10}	5.03×10^{10}	2.36×10^{-5}	Not used
Mo	138	1.22×10^{11}	1.92×10^{11}	4.8×10^{-6}	1.8×10^{7}
SS	14	7.51×10^{10}	1.24×10^{11}	1.73×10^{-5}	1.4×10^{6}

When the cavity is brought under vacuum, the 1.0×10^5 Pa loading of air pressure outside the enclosure causes the cavity to deform. The clamps around the thin weld joint on the outer SS vacuum wall are not included in the simulation models. We force the two sides of the joint fixed in the z-direction in an attempt to account for the clamping force in the structural simulations. The two symmetry planes shown in Figure 12 are symmetric constraints. Assuming the air permittivity in the gun cavity is unchanged with and without the pressure, the displacements due to the atmospheric pressure loading result in -136 kHz and -140 kHz frequency changes in Gun-1 and Gun-2, respectively. The Al end plates and the vacuum wall are treated as fully bonded in the simulations, which make the models stiffer than their actual cases. Removing the Al end plates and the SS center tube behind the cathode, the frequency changes due to the atmospheric pressure in Gun-1 and Gun-2 become -160 kHz and -166 kHz, respectively, which are still stiffer than their actual cases. The simulations suggest that Gun-1 and Gun-2 have similar structural support, which is desired.

Obtaining an accurate estimate of detuning in this case is difficult. One reason is that there are several bolted or clamped connections on the cavity jacket that do not flex in the way that a solid connection would, which is how they are modeled. Without the permittivity effect, the measured frequency shift due to vacuum pressure load should be 236 kHz (=-180-56) [5]. The frequency detuning due to pump down measured at SLAC agrees with the LBNL measurements. The difference between the simulation model and the actual case results in about 100 kHz error for the atmospheric pressure. The simulation results are summarized in Table 9.

Table 9. Frequency Changes due to Atmospheric Pressure without Permittivity Change

Gun	**Simulated Gun-1**	**Simulated Gun-2**	**Measured Gun-1**
dF (kHz)	-136	-140	-236

The displacements for Gun-2 are shown in Figure 13. The atmospheric pressure reduces the accelerating gap, and thus causes a decrease in the cavity frequency.

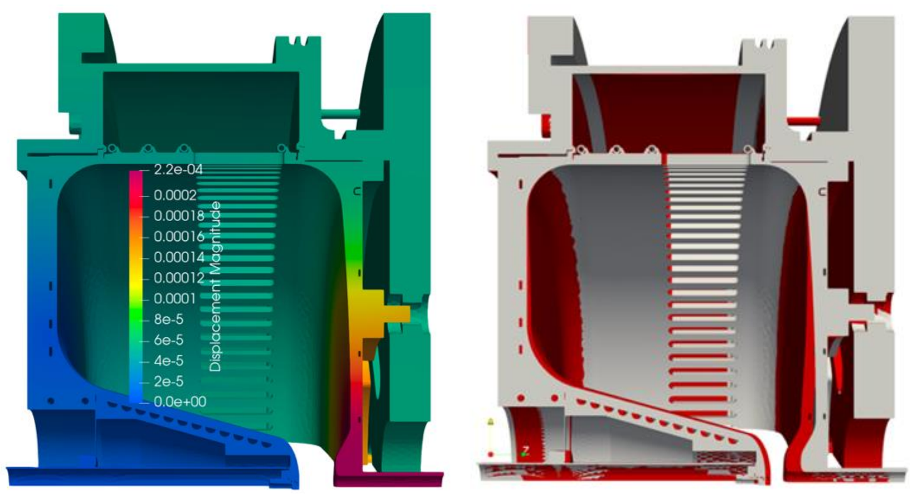

Figure 13: The Gun-2 displacement amplitude (left) and cavities (right) without (grey) and with (red) air pressure. The geometry deformation is scaled 100 times large for visualizing. No air permittivity changing from air to vacuum was assumed in this case.

7. Tuner Sensitivity

There are four motorized tuners attached to four tuner pads on the anode plate (one tuner per pad) that can each pull or push on the plate by up to at least 6 kN. Pushing or pulling the tuners can change the cathode-to-anode gap length, and thus can tune the cavity frequency. The computed cavity frequency changes due to the maximum applied tuner force is 197 kHz in the simplified Gun-2 solid model without Al end plates and the SS center tube behind the cathode nose. The inferred tuner sensitivity is 33 Hz/N, which is close to the 30 Hz/N value measured in Gun-1 [7].

At the worst scenario, the Gun-2 stress fields with air pressure loading plus a 6 kN pushing force from each tuner are shown in Figure 14. The maximum stress on the anode plate is 1.3×10^8 Pa, which occurs on the corner of the beampipe and the anode plate. The Von Mises Stress outside this region is well below 1×10^8 Pa.

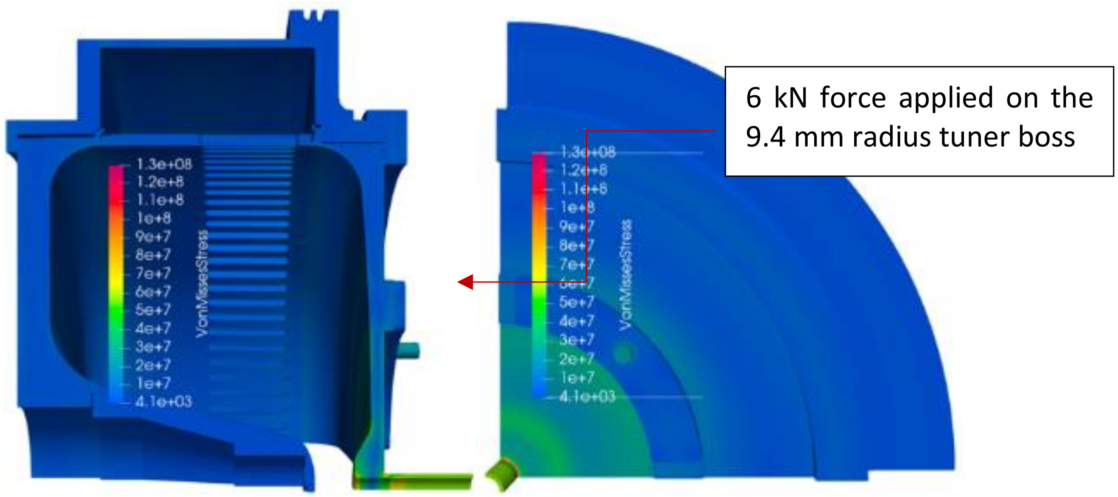

Figure 14: The Von Mises stress in cross section (left) and side view (right) under air pressure loading and a 6 kN pushing force on each tuner in the Gun-2 solid model.

8. RF Heat Load

We assume Gun-2 will operate with a 19 MV/m cathode gradient, similar to Gun-1 (although the gradient may be increased to 20 MV/m). To coarsely tune the cavity frequency with the RF on, the water flow rate in the anode plate can be adjusted: a range of 2.3 gpm to 4.0 gpm is assumed. To reduce the required pull force for Gun-1, the flow rate was reduced to the low end of this range. For Gun-2, we are designing the tuners to push only, and we assume a nominal flow rate of 2.8 gpm to allow some adjustment range if needed (the push-only choice should result in a lower steady state tuner force, and it allows us to use more robust piezo actuators for fine frequency control).

Tables 10 and 11 list the assumed cooling channel water temperatures and transfer coefficients for a total anode flow (into 4 parallel lines) of 2.3 gpm and 4.0 gpm, respectively. The cooling channel IDs on cathode and anode plates starting from 1 to 4 represent the cooling paths from the outer to the center. The air convective heat transfer coefficient depends on air circulation, 10-W/m^2 ^{o}C is taken in the simulations assuming the air temperature of 25^{o}C.

Table 10: Thermal Parameters with a 2.3 gpm Anode Flow Rate

Water inlet T = 30 °C	T(°C)	h (W/m^2 °C)
Cavity wall	35	1.54×10^4
Anode 1 2 3 4	42	6790, 6560, 5710, 5730
Cavity nose cone	35	2.99×10^4
Cathode 1 2 3 4	35	1.96×10^4, 2.03×10^4, 2.37×10^4, 2.52×10^4

Table 11: Thermal Parameters with a 4.0 gpm Anode Flow Rate

Water Inlet T = 30 °C	T(°C)	h (W/m^2 °C)
Cavity wall	35	1.54×10^4
Anode 1 2 3 4	35	13610, 12290, 10610, 10700
Cavity nose cone	35	2.99×10^4
Cathode 1 2 3 4	35	1.96×10^4, 2.03×10^4, 2.37×10^4, 2.52×10^4

The temperature profiles in Gun-2 are shown in Figure 15 with a 20 MV/m gradient at the cathode center for different anode flow rates. One can see that the largest temperature rises occurs on the anode nose for the lower anode flow rate and shifts to the vacuum slot openings for the higher flow rate. There is a 22 W wall loss on the Gun-2 SS inserts for a 750 keV energy gain, mainly dissipated on the anode nose SS insert. The temperature on the anode nose is about 4 ^{0}C higher due to the SS insert in Gun-2 than Gun-1 with a 2.3 gpm anode flow rate.

The detuning caused from the RF heating is mainly due to the outward bowing of the anode plate as it heats up more on the interior side than the exterior side where the cooling channels are located. The clamps around the thin weld joint in the outer wall were not included in the simulation models. We force the two sides of the joint (the arrows pointed to in Figure 12) fixed at z-direction in an attempt account for the clamping force for the RF detuning simulations.

The RF detuning in Gun-1 and Gun-2 from the simulations are summarized in Table 12. There are some observations from the simulations: (1) The RF heating increases the accelerating gap, and thus causes an increase in the cavity frequency; (2) For a 20 MV/m gradient at the cathode center, the power loss in Gun-1 and Gun-2 are 91.5 kW and 86.5 kW, respectively. Based on the Gun-1 measurements, 5 kW power loss can cause about 17 kHz frequency changes (5 kW * 112 N/kW * 30 Hz/N = 16.8 kHz). The simulated frequency increase due to the RF heating for Gun-2 yields values less 20 kHz lower than Gun-1, which is closed to the estimation from the Gun-1 measurements; (3) The flow rate changing from 2.3 gpm to 4.0 gpm can reduce the RF detuning about 72 kHz; (4) The simulation models are stiffener than the actual, and thus the simulated RF detuning is lower than the measured Gun-1 RF detuning.

The resulting temperature changes lead to the cavity deformed. The deformed cavity displacements and the corresponding stress profiles in the Gun-2 solid model with different anode flow rates are shown in Figure 16, and Figure 17, respectively (no air pressure and tuner force were assumed in this case).

Table 12. Frequency Changes due to RF Heating

Room T=25°C, air h=10 W/m^2.K	Simulations with cathode center Ec=20 MV/m	
Anode flow rate	2.3 gpm	4.0 gpm
Gun-1: dF/maxT	150 kHz/73 ^{0}C	78 kHz/63 ^{0}C
Gun-2: dF/maxT	130 kHz/77 ^{0}C	59 kHz/63 ^{0}C

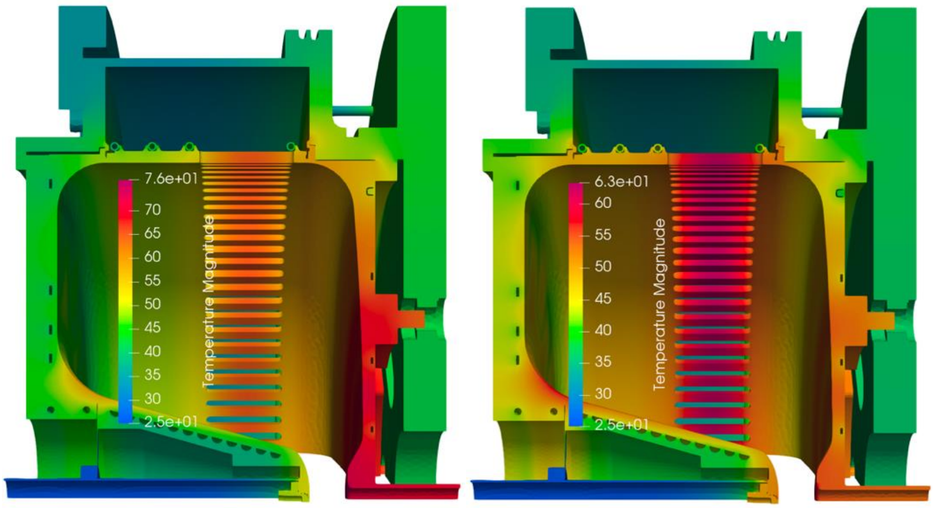

Figure 15: The temperature profiles with a 2.3 gpm (left) and a 4.0 gpm anode flow rates in Gun-2 solid model for a cathode gradient of 20 MV/m.

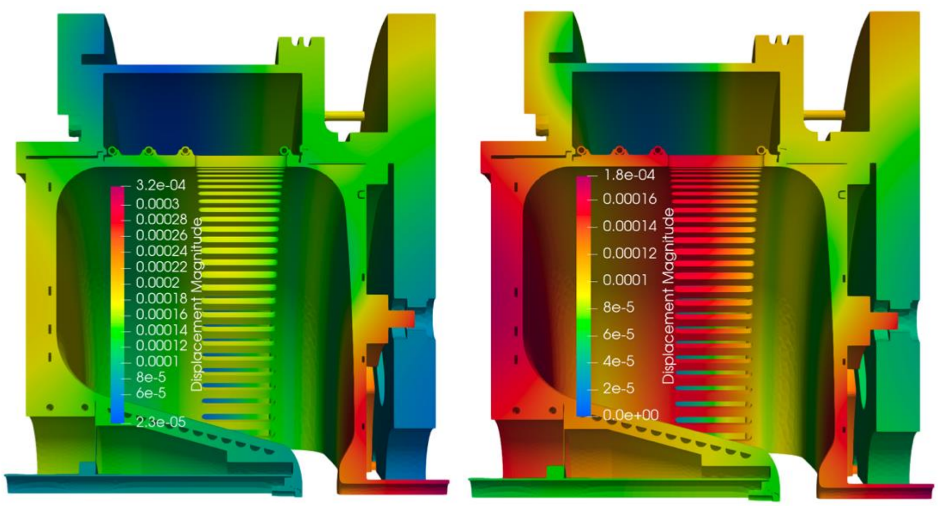

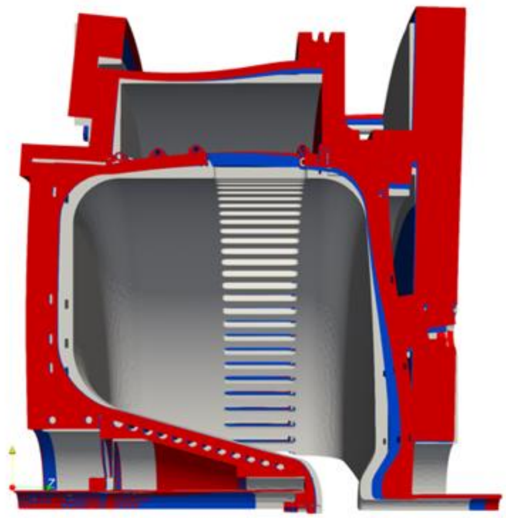

Figure 16: The Gun-2 displacement amplitude profiles for a 2.3 gpm (up left) and 4 gpm (up right) anode flow rates and deformed Gun-2 cavities (down) with a 2.3 (red) and a 4.0 (blue) gpm anode flow rates for a cathode gradient of 20 MV/m. For comparison, undeformed Gun-2 cavity is in grey. The geometry deformations are scaled 100 times large for visualizing.

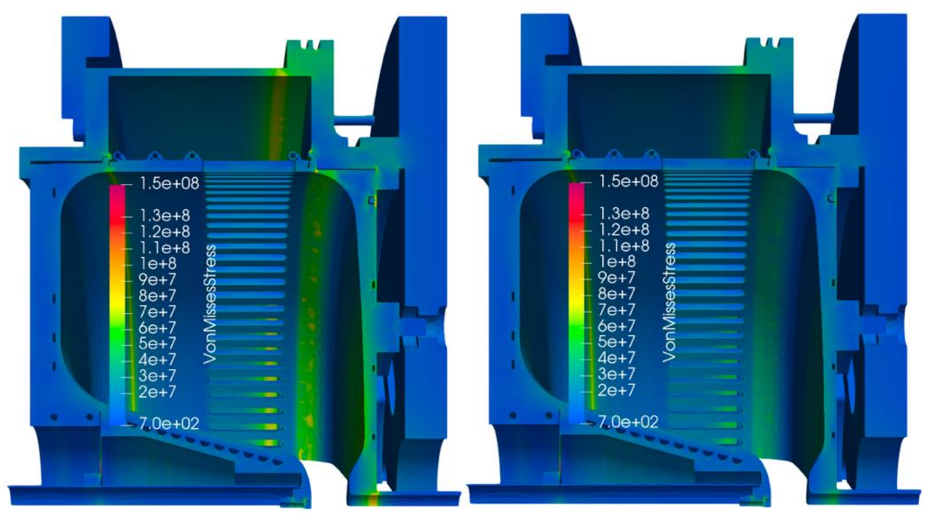

Figure 17: The Von Mise stress profiles in the Gun-2 solid model for a 2.3 gpm (left) and 4 gpm (right) anode flow rates and a 20 MV/m cathode gradient.

Other RF detuning uncertainly includes (1) the water temperature profile along the cooling channels (an estimated average temperature is assumed instead), (2) the heat transfer coefficients (h) on the cooling channels walls, which depends on the water flow rate and other factors and (3) the actual air circulate condition during the gun operation. We expect that the total uncertainty in the cavity frequency correction should be 50 kHz less and the tuners in push mode with 2 kN allow for a total frequency change error of about +/- 60 kHz with the steady state tuner force from zero to 4 kN. The pre-load can also accommodate operation at 5% lower gradient if the frequency change errors are small negative. Similar limits occur for positive frequency errors and higher gradients, but the constraint in this case is the desire to keep the absolute steady state tuner force below 4 kN. If needed, the anode flow rate can be adjusted to offset near +/- 70 kHz errors.

9. Final Prototype Dimensions

The frequency change estimates discussed above were done to provide the information needed to compute the overall frequency change from the 2D geometry, from which the basic shape of the Gun-2 cavity will be fabricated, to the nominal frequency (185.714 MHz) after the initial fast detuning. Since the 2D geometry with a 40 mm cathode-to-anode gap was finalized before the correction calculations were completed, there needs to be a gap length adjustment during machining, which will be done when the cavity frequency is measured before the cathode and anode sections are permanently joined. This machining correction would be done anyway given the uncertainties in the frequency corrections and the machining tolerances. For this purpose, the cathode section will be made 1.17 mm longer than nominal with the expectation that 1.04 mm will be machined off to meet an intermediate target frequency. The numbers are from the current Gun-1 drawings with a starting gap of 41.17 mm before machining.

The frequency accounting connecting the 2D model frequency to the target machining frequency to the nominal operating frequency is summarized in Table 13.

Table 13. Frequency Corrections

Conditions	**Relative Frequency Change (kHz)**	**Absolute Cavity Frequency (MHz)**
Operate gun		**185.714**
Apply 2 kN tuner push force	-60	
Turn RF on after reaching steady state: Ec=19 MV/m, 2.8 gpm anode flow rate	180	
Install cathode plug	-6	
Turn on 30°C LCW: 20°C room temperature	-33	
Pump down including permittivity changes	-180	
Add coupler antennas	40	
Final gap = 40.13mm		**185.773**
Machine anode plate off 1.04 mm	-562	
Build with 1.17 mm longer gap	633	
Fill cavity with air er=1.0006	-56	
Remove cathode plug	6	
Add 3D features but without antennas	-266	
2D Superfish design with er=1		**186.018**

Reading this table from the bottom to top gives the frequency changes that occur as the gun assembly evolves and it is put into operation.

The frequency changes due to the 3D features from the RF simulations are accurate and listed in Table 13. The thermal and structural analysis suggested that Gun-1 and Gun-2 have similar structural support. The Gun-1 measured frequency detuning due to the pump down and the RF heating are listed in Table 13 because we were not able to accurately model them [5] [6]. For 76 kW power loss, the measured Gun-1 RF frequency detuning results are 255 kHz, 228 kHz and 156 kHz at anode flow rate of 2.0 gpm, 2.3 gpm and 2.8 gpm, respectively. Moreover, a 1 kW power change can cause about 3.34 kHz cavity frequency detuning. After power factor correction, for a gradient 19 MV/m at the cathode center (~ 83 kW power loss) in Gun-1, the RF detuning should be 180 kHz listed in Table 13.

10. Effect of the Cathode-to-Anode Gap Length

As shown in Table 14, variations in the gap length of +/- 0.3 mm have little impact on the surface fields in the gun cavity.

Table 14: RF Parameters with Different Gaps

Gap voltage = 750 keV		**Gun-2**	
Frequency (MHz) in 2D shape	185.85	186.02	186.18
Cathode to anode gap length (mm)	39.7	40.0	40.3
Ec (MV/m) at cathode center	20.1	19.8	19.9
Peak E (MV/m) at cavity nose	22.1	21.8	21.9
Peak E (MV/m) near cathode plug opening on cavity nose	21.3	21.0	21.1
Peak E (MV/m) near cathode plug opening on cathode	21.3	21.0	21.1
Peak E (MV/m) at anode nose	21.9	21.6	21.7

The electric field along the beam axis in Gun-2 for different gap lengths is plotted in Figure 18. The small changes in the field profiles were found to have a negligible effect on the injector emittance.

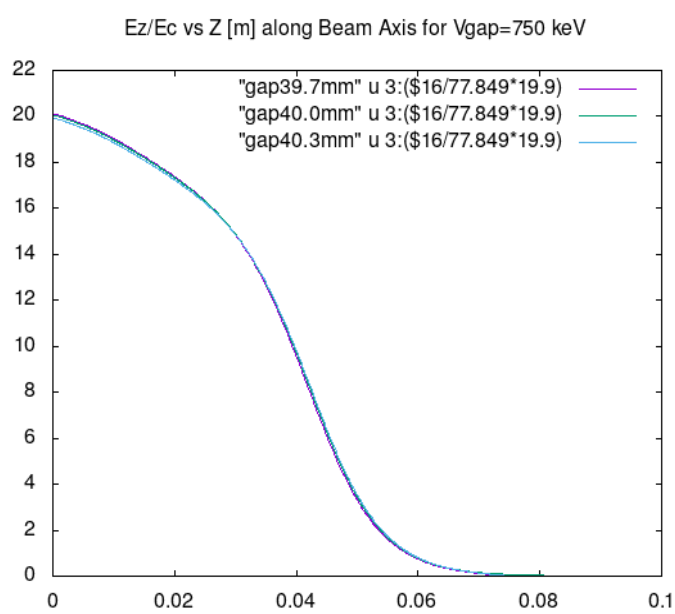

Figure 18: Electric field profile along the beam axis for a 750 keV energy gain with different gap lengths for Gun-2.

11. Multipacting (MP)

In Gun-1, MP in the cavity was not a significant limitation once hydrocarbon contamination was largely eliminated. To see if it would be worse in Gun-2, a search for resonant trajectories for cathode gradients from 25 kV/m to 20 MV/m was done using a 19° azimuthal slice of the Gun-2 model that includes five and a half vacuum slots. No new resonant trajectories were found relative to those predicted in Gun-1 simulations.

MP in the coaxial couplers was initially an issue as well for Gun-1 despite the TiN interior coating and the permanent magnet solenoids that surround the coaxial sections. This was also likely due to contamination, and it did eventually process out although there are still vacuum spikes when the cavity moves far off frequency, which generates higher fields in the coaxial waveguide. We expect it will be no worse in Gun-2 as the coupler design is the same.

12. Summary

Gun-2 RF simulations were performed using a model that includes all the 3D features: vacuum slots, input couplers and probe and view ports. Thermal and structural analyses were done to investigate the effects of the external loading (air pressure and tuner force) and RF heating. No significant issues were found. The most important result is an accounting the difference between the frequency of the basic 2D model on which the gun geometry is based, and nominal frequency during operation. It is critical that this difference be understood so the gun frequency does not end up outside the correction range of the tuners.

References

[1] T. Luo, H. Feng and D. Li, "LCLS-II Spare Gun Preliminary RF Study" presented at SLAC on Sept 28, 2020.

[2] L. Xiao *et al.,* "Spare Gun Multi-Physics Analysis For LCLS-II," in *Proc. Of 12th Int. Particle Accelerator Conf. (IPAC'21), Campinas, Brazil,* May 24-28th, 2021, pp.1688-1691. Doi: 10.18429/JACoW-IPAC2021-TUPAB127

[3] ACE3P code suite. https://conf.slac.stanford.edu/cw18/

[4] F. Zhou, C. Adolphsen, E. Jongewaard, L. Xiao, "AIP Spare VHF-RF Gun", SLAC-I-120-010-R0.

[5] T. Luo, "GunB Electron Gun RF Measurements", LCLSII-2.4-EN-1218-R0.

[6] F. Zhou, "Gun-1 RF Detuning Measurements at SLAC in July 2022" (internal communication).